J. Biomed. Eng. Res.
Vol.26, No.2, 73-86, 2005

Topology Correction for Flattening of Brain Cortex

Min Jeong Kwon, HyunWook Park

Department of Electrical Engineering and Computer Science,
Korea Advanced Institute of Science and Technology,
373-1 Guseong-dong, Yuseong-gu, Daejeon, 305-701, Korea
(Received October 8, 2004. Accepted March 14, 2005)

Abstract: We need to flatten the brain cortex to smooth surface, sphere, or 2D plane in order to view the buried sulci. The rendered 3D surface of the segmented white matter and gray matter does not have the topology of a sphere due to the partial volume effect and segmentation error. A surface without correct topology may lead to incorrect interpretation of local structural relationships and prevent cortical unfolding. Although some algorithms try to correct topology, they require heavy computation and fail to follow the deep and narrow sulci. This paper proposes a method that corrects topology of the rendered surface fast, accurately, and automatically. The proposed method removes fractions beside the main surface, fills cavities in the inside of the main surface, and removes handles in the surface. The proposed method to remove handles has three-step approach. Step 1 performs smoothing operation on the rendered surface. In Step 2, vertices of sphere are gradually deformed to the smoothed surfaces and finally to the boundary of the segmented white matter and gray matter. The Step 2 uses multi-resolutional approach to prevent the deep sulci from geometrical intersection. In Step 3, 3D binary image is constructed from the deformed sphere of Step 2 and 3D surface is regenerated from the 3D binary image to remove intersection that may happen. The experimental results show that the topology is corrected while principle sulci and gyri are preserved and the computation amount is acceptable.

Key words: Cortex, Deformation, Flattening, Intersection, Topology correction

INTRODUCTION

The brain morphology and function in animals have been extensively studied for centuries. However, only limited number of researches for the human brain have been done due to its complex structure, function and the ethical problems. The development of magnetic resonance imaging (MRI) system helps us get valuable information of soft tissues and high-contrast images with non-invasive manner. Fig.1 shows one slice of the 3-dimensional (3D) structural brain magnetic resonance (MR) images obtained by the MRI system. The high spatial resolution of the structural images helps to diagnose the anatomical abnormalities of brain. Since blood oxygenation level dependent contrast (BOLD) was used to image the activated human brain for the first time in 1991 by Ogawa [1], gradient echo (T2*-weighted) BOLD imaging has emerged as the most commonly used functional MRI (fMRI) method due to its improved sensitivity and easy implementation [2].

This work was supported by the 02-PJ3-PG6-EV07-0002, the Ministry of Health and Welfare, Korea.
Corresponding Author: HyunWook Park
Department of Electrical Engineering and Computer Science, Korea Advanced Institute of Science and Technology, 373-1 Guseong-dong, Yuseong-gu, Daejeon, 305-701, Korea
Tel. 042-869-5466, Fax. 042-869-8066
E-mail: hwpark@athena.kaist.ac.kr

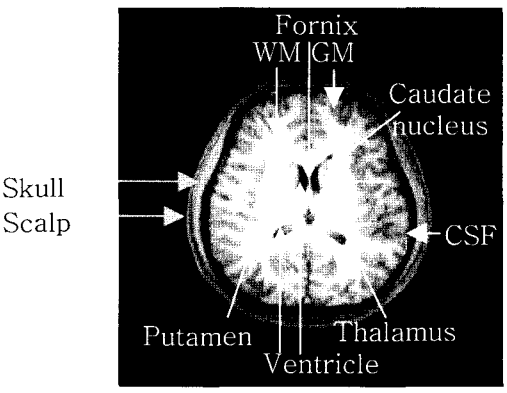

Fig. 1. One slice of structural brain MR image

Fig.2 shows four slices of image obtained by the echo planar imaging (EPI) and Fig.3 shows the activated region mapped on the 2D slices of the EPI image after analysis by BrainVoyager software [3]. Because of low spatial resolution and low contrast of EPI image, it is difficult to locate the activated regions exactly. Hence, to aid the interpretation, the activated regions should be mapped on the 2D slices of high spatial resolution structural images by registration as shown in Fig.4 [3].

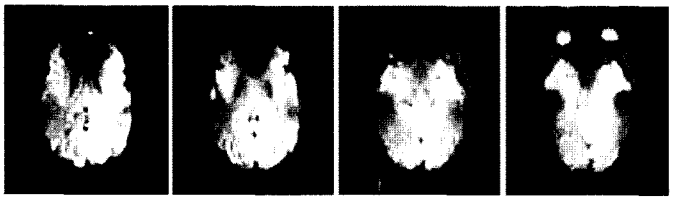

Fig. 2. Four slices of EPI image

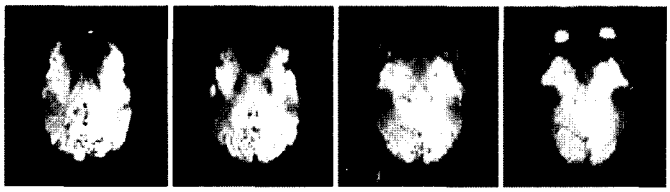

Fig. 3. The activated region mapped on EPI image ($p<0.0035$)

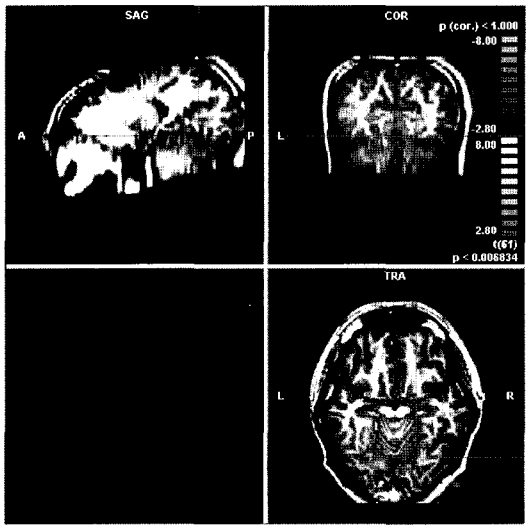

Fig. 4. The activated region mapped on the normalized T1-weighted image

From the 2D slices and the mapped activated regions, user reconstructs the shape of the cortex in his mind. Viewing and understanding is dependent on the number of slices and the slicing direction such as sagittal, axial, coronal, or oblique direction. To observe the 3D relationship with other areas and aid the interpretation, the activated regions are mapped on the 3D rendered surface of cerebral cortex that is the collection of gray matter (GM). Fig.5(b) shows the rendered outer surface of cerebral cortex, which is the boundary between GM and cerebrospinal fluid (CSF) [4]. As shown in Fig.5(b), the human cortex has complex folded pattern that is composed of gyri and sulci for the cortex to grow in the womb and within the limited cranium. The amount about 60-70% of the sulci is buried inside of the cortex [5]. From the outside of the cortex, it is impossible to see the buried sulci as well as the function charted onto them. Besides, the quantitative information between the regions of the cortex is not measured correctly in the 3D stereotaxic coordinates. For example, the distance between two regions that is measured by Euclidean manner is under-estimated than geodesic distance. To resolve these problems, the activated regions are mapped on three flattened surfaces as shown in Fig.5(c), (d), and (e) [4] assuming that the cerebral cortex has the topology of a sphere if the cortical surface is closed at the brainstem [6]. The inflated surface comes directly from the 3D native representation by smoothing its vertices extensively. It gives a similar view of the cortex with the even shape of the sulci and gyri. The spherical representation and the flat map represent the vertices by the spherical coordinates and regular 2D coordinates so that they are useful for the group study and comparison with atlas.

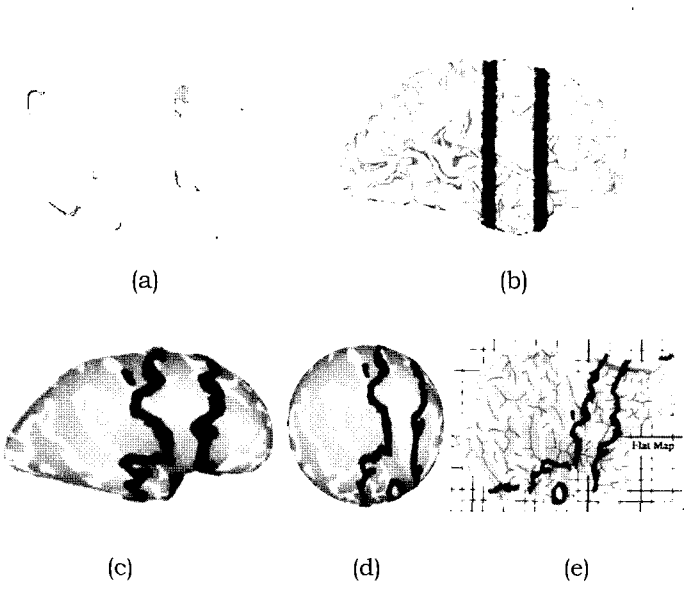

Fig. 5. Surface-based representations [4]: (a) slices, (b) 3D native representation, (c) smoothed surface, (d) spherical representation, and (e) flat map

Flattening algorithm follows three procedures: (1) segmentation of image into white matter (WM), GM, and CSF, (2) surface rendering of boundary between WM and GM to obtain the inner surface of cerebral cortex, (3) correction of topological defects. The surface from rendering usually does not have the topology of a sphere due to the partial volume effect and segmentation error. The topology should be corrected because a rendered surface without a correct topology may lead to incorrect interpretation of local structural relationships, prevent cortical unfolding [7], and not agree with the assumption that the cerebral cortex has the topology of a sphere.

This paper presents a method for topology correction. The proposed method removes fractions beside the main surface and fills cavities in the inside of the main surface by preserving only the set of vertices that are maximally connected. The proposed method also removes handles, which are attached to the main surface like the handle in a cup, by deformation of sphere to the boundary surface of the segmented WM and GM. Topology of sphere is not changed during and after deformation according to the characteristic of parametric deformable models. The method to remove handles is composed of three steps. Three-step approach and multi-resolutional approach are used to follow the narrow and deep concave region. The corrected surface shows that the principle gyri and sulci patterns are preserved with small computation amount.

The kinds of topological defects and the previous methods for correction are described in Section 2. The proposed topology correction method and its experimental results are presented in Sections 3 and 4, respectively. This paper ends with conclusion in Section 5.

PREVIOUS METHODS

The Kinds of Topological Defects

Fig.6 shows one slice where the segmented WM by hierarchical fuzzy c-means algorithm (HFCM) [8] is represented in blue color with the T1-weighted image. Fig.7 shows the rendered surface of the segmented WM by modified marching cubes (MMC) algorithm [9]. There are three topological defects. First, ventricles and sub-cortical structures such as putamen, thalamus, etc, result cavities (e.g., the empty space inside a tennis ball) indicated as red circles as shown in Fig.6 because voxels in those structures do not have the intensity of WM. Cavities are in the inside of the cerebral cortex and are not seen from the outside of surface in Fig.7. Second, fractions indicated as ***A*** circle as shown in Fig.7 happen beside the main surface. The cavities and fractions result in multiple sets of meshes that are disconnected each other by their vertex connectivity and lead to the different topology compared with a sphere. Third, there are handles (e.g., the handle of a cup) in surface indicated as ***B*** circle as shown in Fig.7.

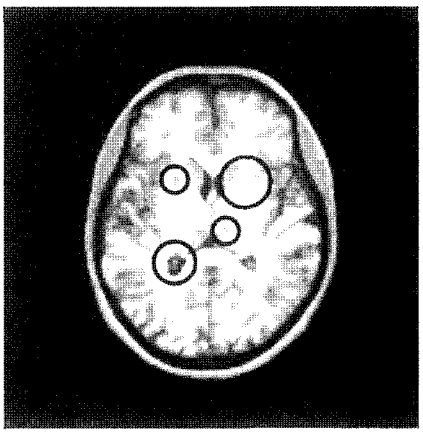

Fig. 6. One slice of structural brain MR image and its segmented WM in blue color

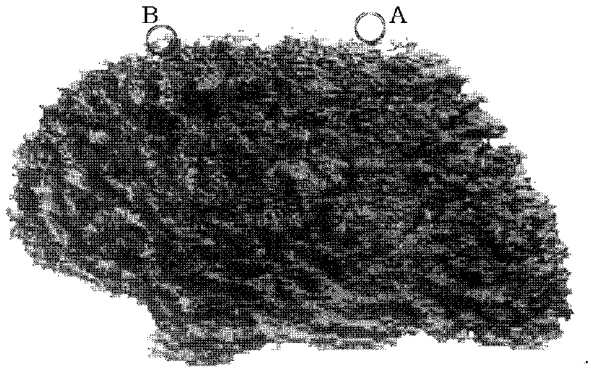

Fig. 7. The rendered surface of the segmented WM in Fig.6

Previous Methods for Topology Correction

There are two types of flattening algorithms. First, the surface is flattened after the rendered surface itself or the 3D volume data of the segmented WM is corrected topologically [6,7,10,11,12,13,14,15,16]. Second, the model surface, which is correct topologically such as a sphere, is deformed to the segmented WM using parametric deformable model [17]. The parametric deformable model preserves the initial topology during and after the deformation so that the topology correction is not required.

Topology Correction in Volume or Surface

Existence of the topological errors can be detected by calculating the Euler characteristic χ [7] or genus g [16] from surface by

$$\chi = V - E + F$$
$$g = 1 + \frac{1}{4}(F - 2V) \quad (1)$$

where V, E, and F is the number of vertices, edges, and triangles of a surface, respectively. A surface is topologically equivalent to a sphere when χ=2 or g=0 while χ is reduced by two or g is reduced by one per each topological error. Teo et al. commented that χ does not yield the exact locations but only the happening of the topological errors. They filled cavities by repeatedly initiating the flood-filling algorithm from non-white matter voxels and removed handles by hand-editing or readjusting the parameters used to obtain WM classification [18].

To correct topology automatically, there are two types of algorithms that are voxel-based and surface-based. Voxel-based algorithm fills or removes voxels in 3D volume data before rendering [6,7,10,11,16]. Surface-based algorithm finds the vertices where there are topological defects and reconstructs vertices so that the surface has the topology of a sphere [13,14,15]. Xu et al. made cortical surface topologically correct by three steps: (1) removal of the extraneous connected structures manually by removing hippocampal formation and filling the ventricles and the putamen, (2) selection of the largest mesh among multiple meshes that are physically disconnected each other, (3) removal of handles by an iterative process of median filtering of a volume data and isosurface generation until χ equals two [7]. The manual removal of extraneous structures is not appropriate to the automatic algorithm. The iterative process is computationally intensive because it requires repeated re-tesselation and filtering [16]. The use of median filtering affects the entire volume and can smooth certain aspects of the cortex [6]. The use of a 3×3×3 median filter does not guarantee a topologically spherical result [6].

Shattuck and Leahy localized the change to specific areas of its topological defects by graph-based algorithm [6]. They formed the connectivity graphs of foreground and background in direction of each x, y, and z slice-by-slice. Each node corresponds to the connected voxels in a slice. The weight of an edge is the number of the intersected voxels for two nodes of the edge between slices. The connectivity is based on D6 for foreground and D18 for background as shown in Fig.8. They assumed that handles tend to make cycles in a graph although it is not proved. They figured out whether there are cycles in each graph, determined whether the node in a graph is removed or not by the three rules, and removed or filled the voxels corresponding to the node in a foreground or background connectivity graph if the node should be removed. The graph-based algorithm does not consider the correct anatomical meaning so that they removed nodes if the number of voxels corresponding to the node is equal or under the specified threshold. The algorithm was performed for background after foreground in z, y, and x direction successively for both connectivity graphs with increasing threshold from 1 until there are no changes. If any graph still had cycles because the candidate nodes to be removed do not satisfy rules for removal, the duplicate slices were used in the slices where there are cycles. The algorithm is only for removal of handles so that they required the initial 3D volume data without cavities and fractions. The cuts are not natural since they can only be oriented along the Cartesian axis and slice duplication is required [11]. The results are dependent on the sequence of slicing direction. For example, the results are different if the sequence is y-x-z or x-z-y. The results are different if correction is performed for background first and foreground second. The sorting sequence of nodes that have the same number of voxels may lead to different maximal spanning tree and different results. The use of threshold only reduces the large change that removes the voxels meaningful anatomically as they said [11]. A cut might happen in wrong place in a handle because the algorithm does not imply the information of volume such as intensity.

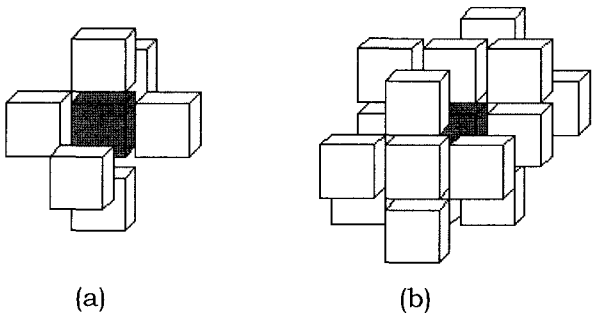

Fig. 8. Connectivity rules: (a) D6 and (b) D18

Fischl et al. corrected topology from the rendered surface. They left the surface geometry essentially unchanged, except in regions containing topological defects [13]. The vertices between a flattened surface to a sphere and the sphere are one-to-one if the surface has the same topology of a sphere. The triangles of a flattened surface are overlapped each other, otherwise. The locations of topological defects are found as the vertices that compose the overlapped triangles of the

flattened surface. The regions where there are the topological defects are re-tessellated. This method is slow because of the flattening step. Removal of overlapping triangles generally removes a much larger part of the surface than is actually necessary in order to achieve the correct topology [11]. The algorithm is only for removal of handles so that they required the initial 3D volume data without cavities and fractions.

Parametric Deformable Models

Parametric deformable models represent curves or surfaces explicitly in their parametric forms. The most well known model is the active contour (snakes) model [19]. The initial contour is deformed to the image by minimization of the following energy [19]:

$$E = \int_0^1 E_{int}(\mathbf{v}(s)) + E_{ext}(\mathbf{v}(s))ds$$
$$E_{int}(\mathbf{v}(s)) = \left(\alpha|\mathbf{v}_s(s)|^2 + \beta|\mathbf{v}_{ss}(s)|^2\right)/2 \quad (2)$$

where $\mathbf{v}(s)=(x(s), y(s))$ is the position of the contour, $\mathbf{v}_s(s)$ and $\mathbf{v}_{ss}(s)$ are the first and the second derivatives of $\mathbf{v}$ with respect to s, respectively. α and β control the elasticity and rigidity of the contour, respectively. E_{int} is the internal energy of the spline due to bending and E_{ext} is the external energy that pulls the contour to the desired position.

It can be shown that the deformable contour minimizing the energy E in eq. (2) can be obtained by finding the steady-state solution of the following dynamic equation [7]:

$$\Delta\mathbf{v} = \lambda_{int}F_{int} + \lambda_{ext}F_{ext}$$
$$F_{int} = \alpha\nabla_s^2\mathbf{v} - \beta\nabla_s^2\left(\nabla_s^2\mathbf{v}\right) \quad (3)$$
$$F_{ext} = -\nabla E_{ext}$$

where $\mathbf{F}_{int}$ is the internal force and $\mathbf{F}_{ext}$ is the external force corresponding to the internal energy and the external energy, respectively. λ_{int} and λ_{ext} control $\mathbf{F}_{int}$ and $\mathbf{F}_{ext}$, respectively.

Given an initial contour or surface, the model deforms iteratively until it converges as follows:

$$\mathbf{v}_k^{t+1} = \mathbf{v}_k^t + \Delta\mathbf{v} \quad (4)$$

where $\mathbf{v}_k^t$ is the coordinates of k^{th} vertex at t^{th} iteration.

For example, consider Data 1 where the matrix size is 256×256×256. Data 1 is made of the same 100 2D slice images in Fig.9(a) where the object is represented in gray color and empty space for the other slices. The rendered surface is shown in Fig.9(b). Let's consider that the initial surface is set as a sphere that includes the object in Fig.9(d). The radius is the distance of the maximally distant vertex in the Fig.9(b) from the center of all vertices. The initial surface is seen in one slice as a yellow line in Fig.9(c) and it shows the initial surface implies the object. The number of vertices and triangles are 10242 and 20480, respectively.

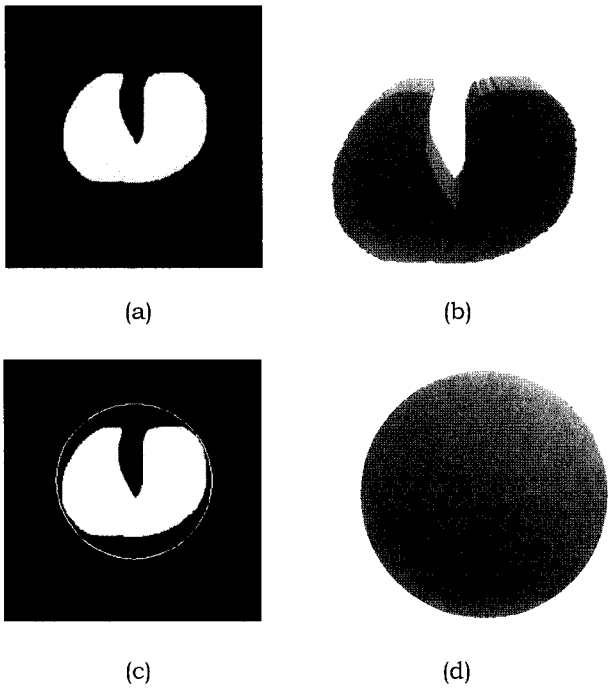

Fig. 9. Data 1: (a) one slice, (b) rendered surface of the object, (c) the initial surface in one slice, and (d) the initial surface in 3D

The initial surface is deformed to the object as shown in Fig.10(a) under $\mathbf{F}_{ext}$ designed by the edge information using Sobel operator [20] as follows:

$$\mathbf{F}_{ext}(\mathbf{v}) = \mathbf{F}_{edge}(\mathbf{v}) = \lambda_{edge}\begin{pmatrix}\partial I(\mathbf{v})/\partial x \\ \partial I(\mathbf{v})/\partial y\end{pmatrix} \quad (5)$$

where $I(\mathbf{v})$ is the intensity value in image at $\mathbf{v}$ and λ_{edge} controls the external force by the edge information. The deformed surface is not converged to the object

because the initial surface is far from the object. If $\mathbf{F}_{ext}$ is smoothed by gaussian filter with σ of 1 to enlarge the capture range of the surface [19], the deformed surface in Fig.10(b) is converged to the object more than in Fig.10(a). The external force should be controlled for $\Delta\mathbf{v}$ not to exceed one voxel and not to pass edge [21] so that α, β, λ_{int}, λ_{ext}, λ_{edge}, and the number of iteration are set as 1, 0, 1, 1, 1, and 100, respectively in both Fig.10(a) and Fig.10(b).

In case the initial surface is far from the target object, the external force like pressure force can be used to extend the capture range of the model. Pressure force directs vertex to its normal vector $\mathbf{n}$ [21] as follows:

$$\mathbf{F}_{ext}(\mathbf{v}) = \mathbf{F}_{balloon}(\mathbf{v}) = \lambda_{balloon}\mathbf{n}(\mathbf{v}) \tag{6}$$

Surface is inflated or deflated by the sign of $\lambda_{balloon}$. If $\mathbf{v}$ is in the inside of the object (this can be detected by the intensity in image) $\lambda_{balloon}$ is positive to inflate the contour. Otherwise, $\lambda_{balloon}$ is negative to deflate the surface [8]. In Fig.10(c) and (d), $\mathbf{F}_{ext}$ is designed by $\mathbf{F}_{balloon}$ with $\lambda_{balloon}$ set as 0.5 and 0.1, respectively. If the average difference between the deformed and the previously deformed surfaces is equal or less than 10%, deformation stops. The number of iteration is 207 and 529 in Fig.10(c) and (d), respectively. Deformation is dependent on the value of parameters. If $\lambda_{balloon}$ is as large as in Fig.10(c), the vertices are deformed fast and well toward the deep concave region, however, the nearby vertices intersect each other because the vertices are deformed locally. The surface in Fig.10(d) does not show the intersection between vertices, however, the vertices do not deform to the concave region because they fall in local minima.

To pull the model to the desired concave region without intersection, additional external force such as gradient vector flow [7] and self-proximity term [17] is used. Xu et al. did not consider the intersection problem [7]. MacDonald et al. showed that intersection does not happen after deformation, however, they needed to calculate the distances between vertices at every iteration and required much computation amount although they used multi-resolutional approach [17].

In parametric deformable model, the design of the external force, the control of parameters, and the intersection between vertices should be considered carefully for good deformed surface and low computational cost. Especially in flattening of sphere in brain MR images, the external force should be designed for vertices to be pulled into the deep and narrow sulci and intersection between vertices should be removed.

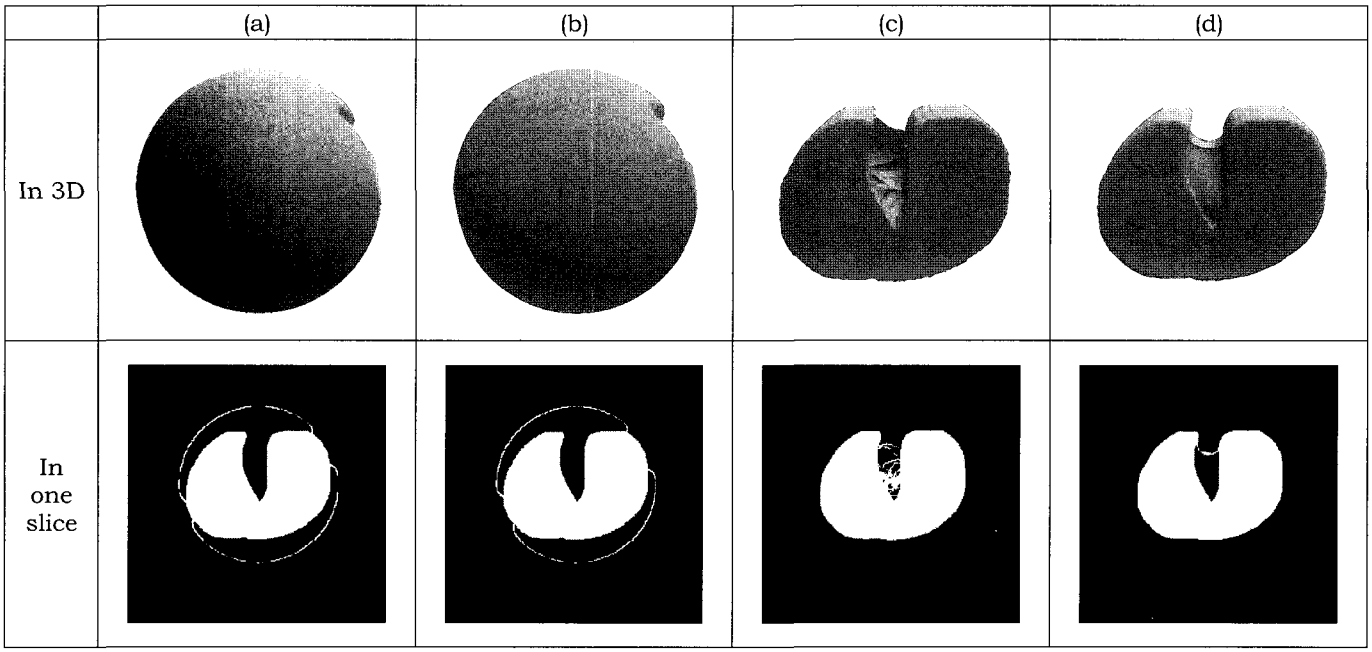

Fig.10. The deformed surface for Data 1 with: (a) F_{edge}, (b) F_{edge} smoothed by gaussian filter, (c) $F_{balloon}$ when $\lambda_{balloon}$ is 0.5, and (d) $F_{balloon}$ when $\lambda_{balloon}$ is 0.1

PROPOSED METHODS

Observation in Parametric Deformable Model

A sphere is deformed to Data 2 by $\mathbf{F}_{int}$ and $\mathbf{F}_{balloon}$ with α, β, λ_{int}, λ_{ext}, and $\lambda_{balloon}$ that are set as 1, 0, 1, 1, and 0.5, respectively as shown in Fig.11. Data 2 has broad and shallow concave region. Sphere is deformed well to the object as shown in Fig.11(b) with the iteration number of 97. From this, we can guess that sphere can be deformed well to the object if it has shallow and broad concave regions.

From a sphere to Data 3 as shown in Fig.12(a), the vertices intersect each other as shown in Fig.12(b) because the object has deep concave region. Fig.12(c) shows the rendered surface smoothed by the number of 1000 by only $\mathbf{F}_{int}$. The smoothed surface is deformed to the object in Fig.12(a) by $\mathbf{F}_{int}$ and $\mathbf{F}_{balloon}$ with α, β, λ_{int}, λ_{ext}, and $\lambda_{balloon}$ that are set as 1, 0, 1, 1, and 0.5, respectively as shown in Fig.12(d). The smoothed surface is deformed well to the object with the iteration number of 24 without intersection. From this, we can guess that the deformation between similar surfaces such as the smoothed surface and the original surface is performed well.

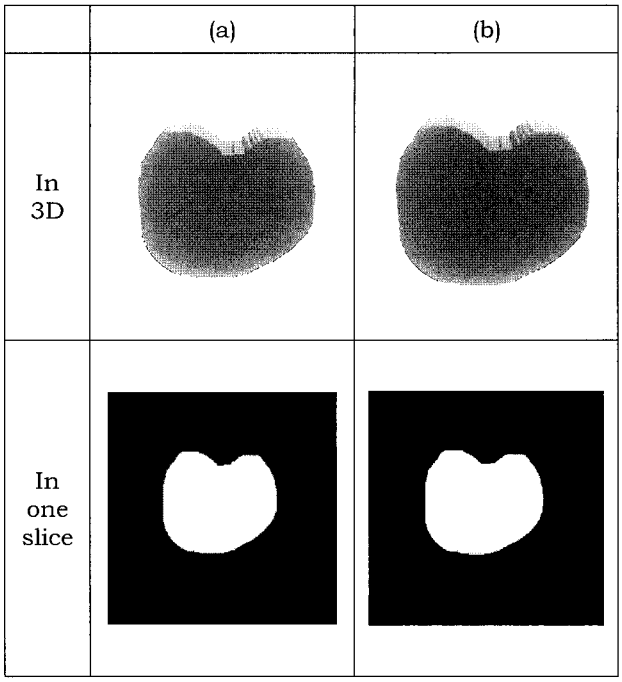

Fig. 11. Deformation of surface for Data 2: (a) the rendered surface and (b) the deformed surface

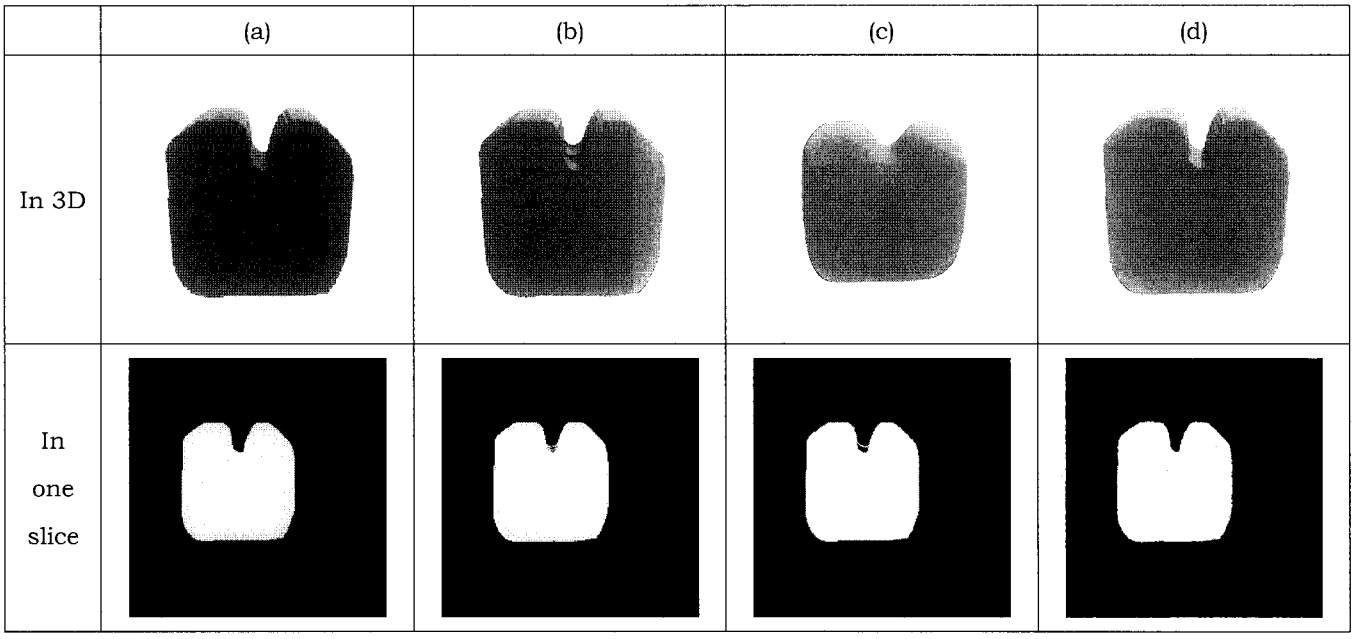

Fig. 12. Deformation of surface for Data 3: (a) the rendered surface, (b) the deformed surface, (c) the smoothed surface (a), and (d) the deformed surface from the smoothed surface

The Proposed Method for Topology Correction

From two observations, topology of surface can be preserved by deformation from a sphere to largely smoothed surface (S_N) of the rendered surface, from largely smoothed surface (S_N) to less smoothed surface (S_{N-1}) successively, and from the smallest smoothed surface (S_1) to the rendered surface (S_0) after all as follows:

Step 1: $S_0 \rightarrow S_1 \rightarrow \ldots \rightarrow S_{N-1} \rightarrow S_N$
Step 2: sphere $\rightarrow S_N \rightarrow S_{N-1} \rightarrow \ldots \rightarrow S_1 \rightarrow S_0$

Step 1 is the smoothing step to make smoothed surfaces by only $\mathbf{F}_{int}$ and Step 2 is the deformation step from sphere to surfaces successively by $\mathbf{F}_{int}$ and $\mathbf{F}_{balloon}$.

If the object in volume data has very deep concave region, the largely smoothed surface (S_N) also has deep concave region so that a sphere cannot be deformed well without intersection of vertices. For example, the rendered surface in Fig.9(b) is smoothed largely with the number of 1000 as shown in Fig.13(a). Deformation from a sphere to the largely smoothed surface results in intersection as shown in Fig.13(b) and (c). This is resolved using multi-resolutional approach in deformation from a sphere to S_N in Step 2.

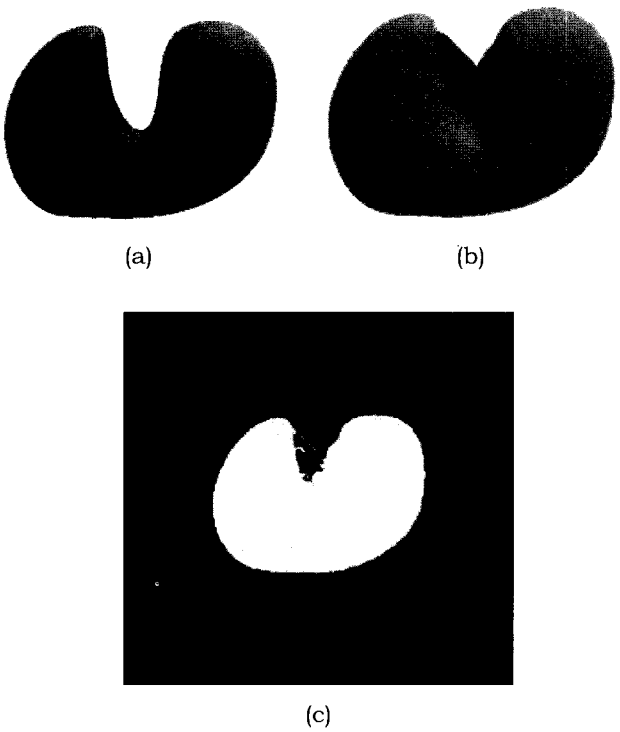

Fig. 13. Deformation of surface of Fig.9(b): (a) the smoothed surface, (b) the deformed surface in 3D, and (c) the deformed surface in one slice

The overall block diagram of the proposed method is shown in Fig.14. Topology is corrected from the rendered surface by removal of cavities and fractions and by removal of handles. The method to remove handles is performed in three steps.

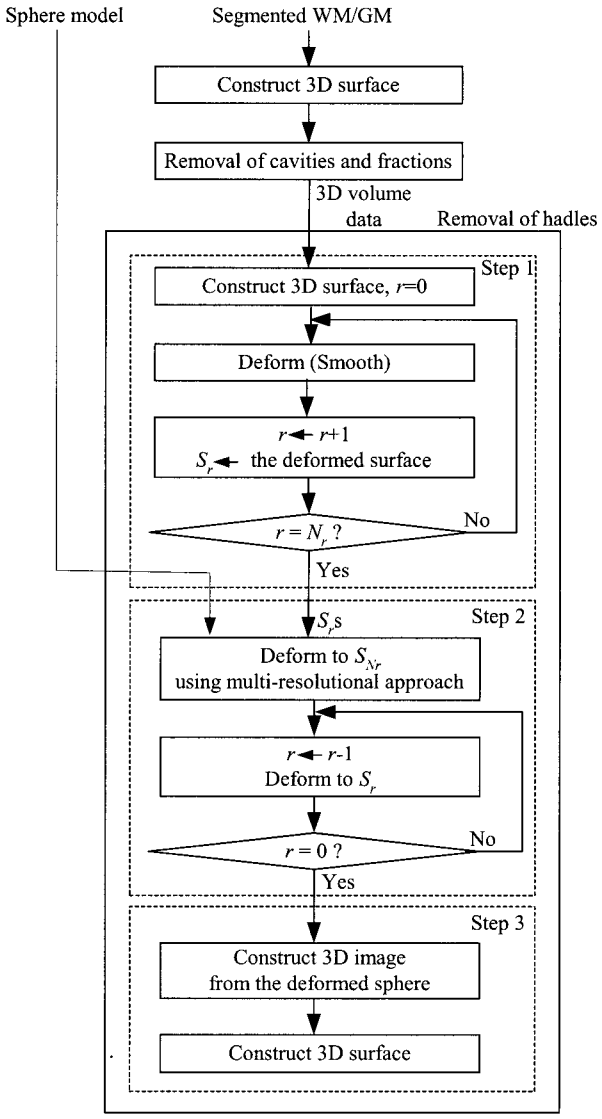

Fig. 14. The overall block diagram

Pre-Processes

The boundary surface of WM and GM can be constructed by a surface rendering algorithm after segmentation of brain MR image. Although the proposed method for topology correction is independent from the methods for segmentation and

surface rendering, the HFCM algorithm [8] and the MMC algorithm [9] are used for segmentation and surface rendering, respectively. The HFCM algorithm segments T1-weighted image into WM, GM, and CSF even if the image has inhomogeneous distribution of intensity in the same tissue due to system noise such as RF nonuniformity and partial volume effect. The MMC algorithm makes triangle primitives and their vertices from the segmented WM volume data.

The proposed method requires a sphere model as an input. The sphere model is the one refined by subdividing one triangle into four smaller ones from a simple sphere model with 20 triangles and 12 vertices [22]. The sphere model has 320 triangles and 162 vertices and is shown in Fig.15.

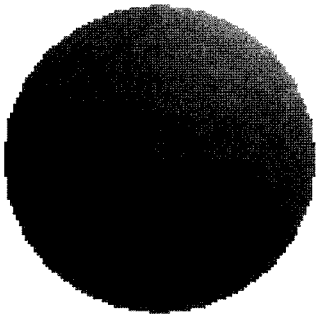

Fig. 15. The sphere model

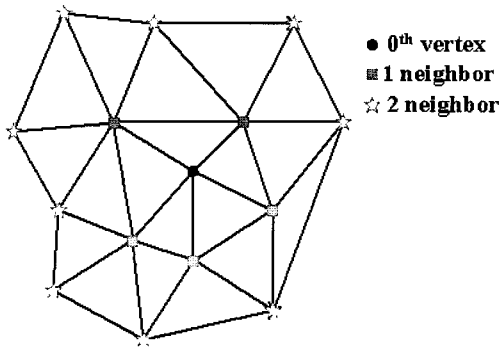

Fig. 16. The connected vertices

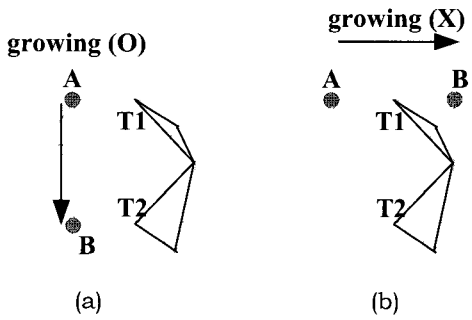

Fig. 17. Growing of grid points

Removal of Fractions and Cavities

From one vertex, vertices are connected each other as its neighbors in surface as shown in Fig.16. As Xu et al. did [7], fractions are removed by removal of vertices that are not implied in the set where the number of elements is the maximum. However, if cavities adjacent to the surface that has the maximum number of vertices, the vertices of cavities is not removed so that cavities survive. To remove these cavities, grid points from the outside of the surface are grown to the inside of the surface. The growing stops when the line segment between the grown point and the growing point from the grown point meets any triangle. For example, if Point B is grown from Point A in Fig.17, the line segment constituted of Point A and Point B does not meet any triangle in Fig.17(a) so that Point B becomes the grown point. On the other hand, the line segment between Point A and Point B in Fig.17(b) meets triangle T1 so that B point cannot be a grown point. If all growing process stops, the non-grown voxels are the voxels in the inside of the surface and constitute object so that surviving cavities are removed by filling their voxels as an object. After obtaining of the new object, the surface is newly rendered.

Removal of Handles

In Step 1, the vertices of the rendered surface are iteratively smoothed and the deformed surface is stored as S_r. r begins at zero and increases by one at the interval of the defined number of iteration N_t. When r reaches N_r, the smoothing process is stopped. The surface is the boundary surface between the segmented WM and GM at r=0 and is smoothed more as r increases. The smoothing process is performed using only $\mathbf{F}_{int}$ with α, β, and λ_{int} that are set as 1, 0, and 1, respectively.

In Step 2, vertices of the sphere model is iteratively deformed to the surfaces S_r from r=N_r to r=0. The topology of sphere is preserved under deformation of parametric deformable model. Intersection can be reduced during deformation between the similar surfaces in Step 2. The deformation is performed using $\mathbf{F}_{int}$ and $\mathbf{F}_{balloon}$ with α, β, λ_{int}, λ_{ext}, and $\lambda_{balloon}$ that are set as 1, 0, 1, 1, and 0.5, respectively. To make the deep concave region in S_{Nr} to be shallow region, multi-resolutional approach is used from sphere to S_{Nr}. Multi-resolutional approach is a method that is performed from low-resolution at level 0 to high-resolution at level (L+1) as shown in Fig.18 [23].

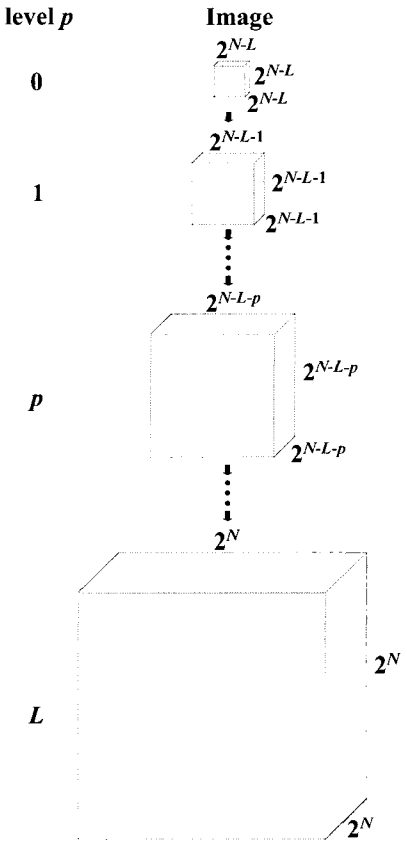

Fig. 18. Multi-resolutional approach

The high-resolution image is decimated to make the image of one lower level. This makes the deep concave region to be the shallow region. In general, the narrow concave region in the high-resolution image is removed in the low-resolution image. However, the deformed surface has the broad region rather than the narrow concave region since the surface is smoothed sufficiently at $r=N_r$. The sphere model is deformed to the lowest-resolution surface using the lowest resolution image. And then, the sphere model is refined by subdivision to have the increased number of triangles and vertices. The refined surface is deformed using one-level higher resolution image. Deformation and refinement are performed iteratively. At scale p, the size of image is $(2^{N-L-p}\times 2^{N-L-p}\times 2^{N-L-p})$, the number of triangles is $(320\cdot 4^{(L-p)})$, and the number of vertices NV_p is $(NV_{(p-1)}+(NV_{(p-1)}+320\cdot 4^{(L-(p-1))}))$. If L is 3 and the surface of Fig.13(a) is the target surface, Fig.19(a) shows the one slice of the volume data according to the resolution. The finally deformed surface from sphere model to the surface of Fig.13(a) is shown in Fig.19(b) and (c), which show that deformation is performed well and there is no intersection.

The finally deformed surface does not guarantee that there is no intersection. Intersection may happen if the change of surfaces is abrupt and the effect of external force is large. Intersection causes cavities inside the surface like holes caused by intersection in 2D as shown in Fig.20. In Step 3, a 3D binary volume data is acquired from the deformed sphere by growing of grid points from the outside to fill the cavities. Then, the new surface from the acquired volume data is rendered and does not imply intersection.

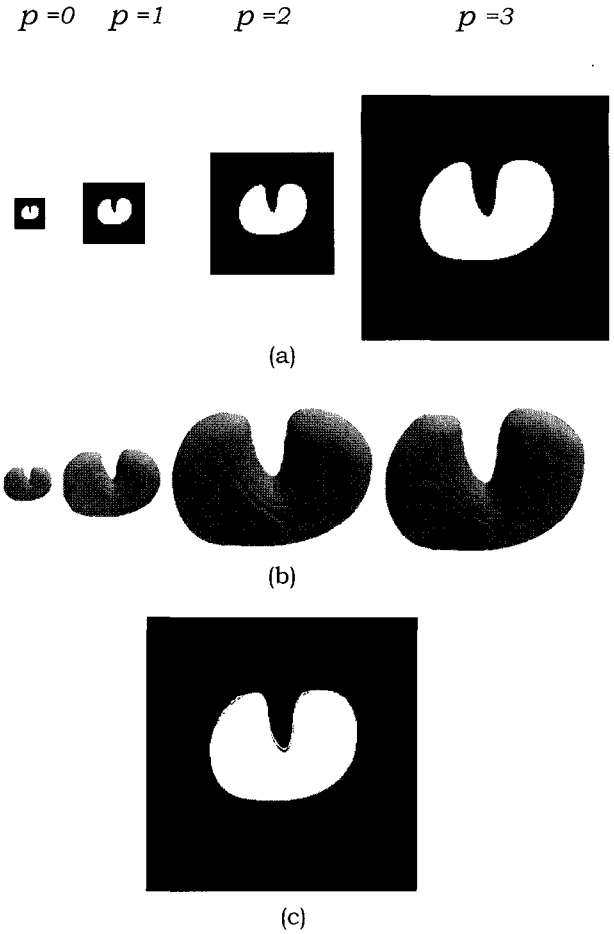

Fig. 19. Deformation of sphere to the surface of Fig.13(a) when $r=Nr$ is in Step 2: (a) one slice according to the resolution, (b) the deformed surface according to the resolution in 3D, and (c) the deformed surface at p=3 in one slice

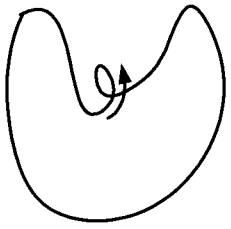

Fig. 20. Hole caused by intersection in 2D

EXPERIMENTAL RESULTS

The experiments were performed in 2 GHz Pentium IV with 512 MB memory using Visual C++. Data 4 was a sample data of the BrainVoyager [3] from a Siemens 1.5 Tesla MRI system and was a T1-weighted image. For Data 4, TR was 9.7*ms*, TE was 4.0*ms*, and the matrix size was 256×256×256. Data 5 was obtained by a 3D magnetization prepared rapid acquisition gradient echo technique (MP-RAGE) from an ISOL 3.0 Tesla MRI system at the KAIST fMRI laboratory, Korea. For Data 5, TR was 10*ms*, TE was 4.0*ms*, and the matrix size was 256×256×256. The two slices of Data 4 and Data 5 and their segmented WM, GM, and CSF by HFCM [8] are shown in Fig.21. The rendered boundary surfaces of the segmented WM and GM for the left brain in Data 4 and Data 5 by MMC [9] are shown in Fig.22.

After preserving only the set of vertices that are maximally connected among sets of vertices and growing of grid points from outside to the inside of surface, the surfaces for the left brain in Data 4 and Data 5 are shown in Fig.23. The corrected surfaces do not have fractions as shown in Fig.23. Cavities in the inside of the surfaces are filled for each segmented left WM data represented in gray color as shown in Fig.24.

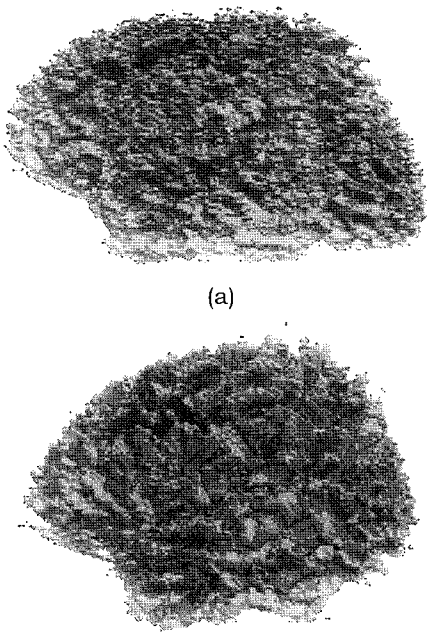

Fig. 22. The rendered boundary surface between the segmented WM and GM: (a) Data 4 and (b) Data 5

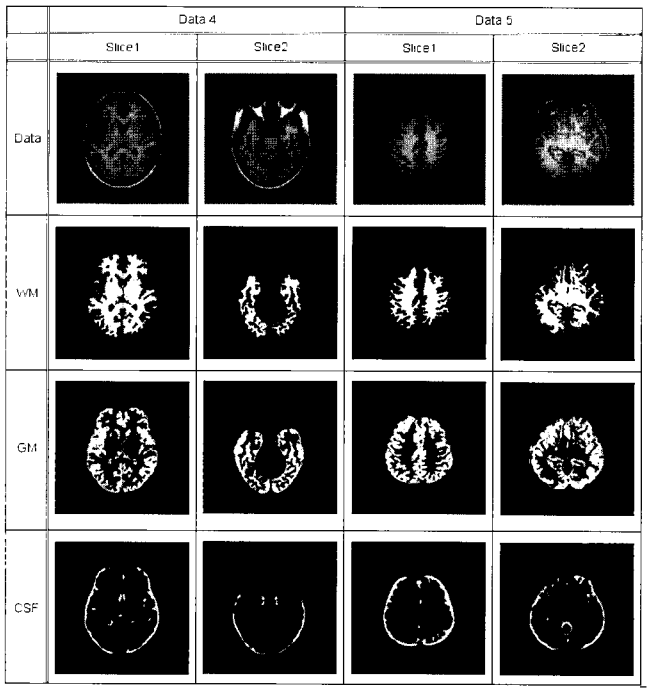

Fig. 21. Two slices of Data 4 and Data 5 and their segmented WM, GM, and CSF

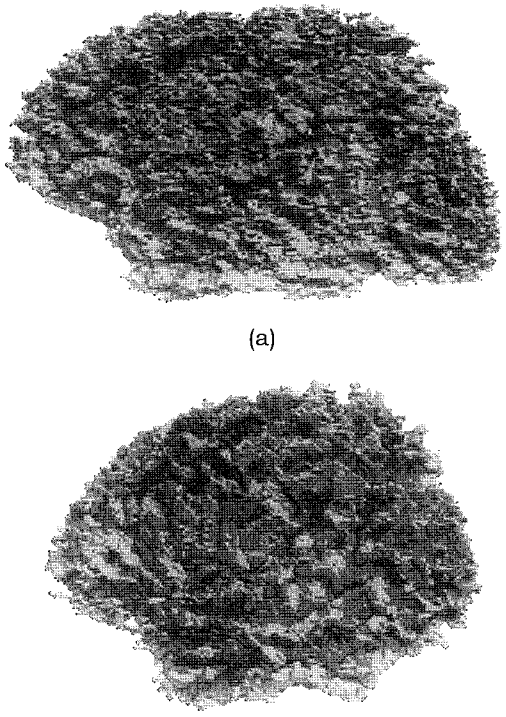

Fig. 23. The corrected surface after removal of cavities and fractions: (a) Data 4 and (b) Data 5

To remove handles, we selected the parameters that N_t =100, N_r=10, S=3, the number of iteration of deformation of Step 2 is 300 in p=0 at r=N_r and 50, otherwise. Fig.25 shows the gradual deformation process in Step 2 from a sphere to the corrected surfaces after removal of cavities and fractions for Data 4 and Data 5. There are no triangles intersected other triangles in the finally deformed surfaces after Step 2 for Data 4 and Data 5 .

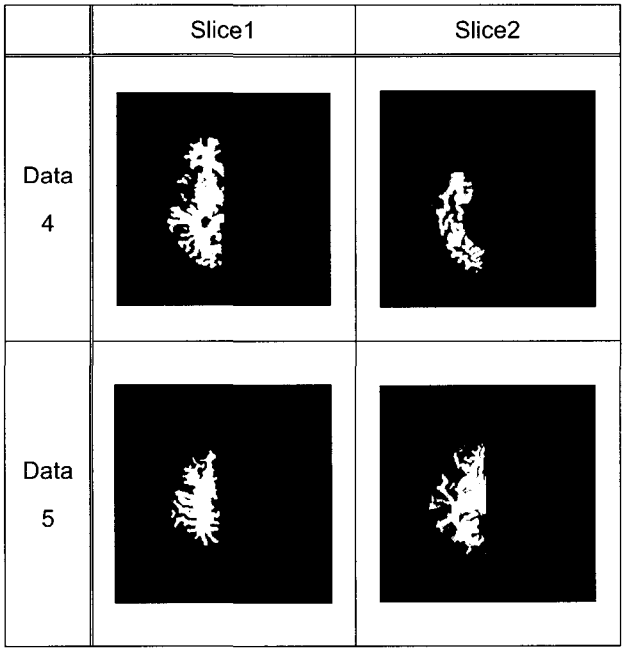

Fig. 24. The corrected surface in yellow line and the segmented WM in gray color after removal of cavities and fractions in two slices for Data 4 and Data 5

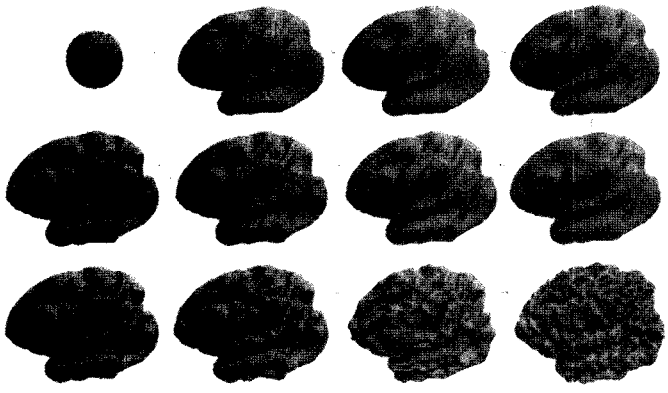

(a)

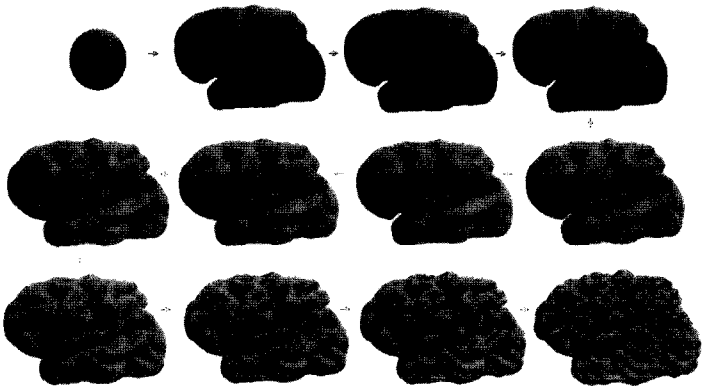

(b)

Fig. 25. Gradually deformed surface in Step 2: (a) Data 4 and (b) Data 5

Therefore, it is not necessary to construct new surface from the 3D binary volume data obtained by growing grid points from the outside to the inside of the finally deformed surface after Step 2. The finally corrected surfaces are in 3D in Fig. 26 and in two slices in Fig.27. To compare the proposed method, the result by the algorithms of Xu et al. [7] and Shattuck and Leahy [6] are also shown in Fig.26 and Fig.27. Algorithm by Shattuck and Leahy requires much computation time until there is no cycle in both graphs, the process is stopped manually when the number of iteration is 20.

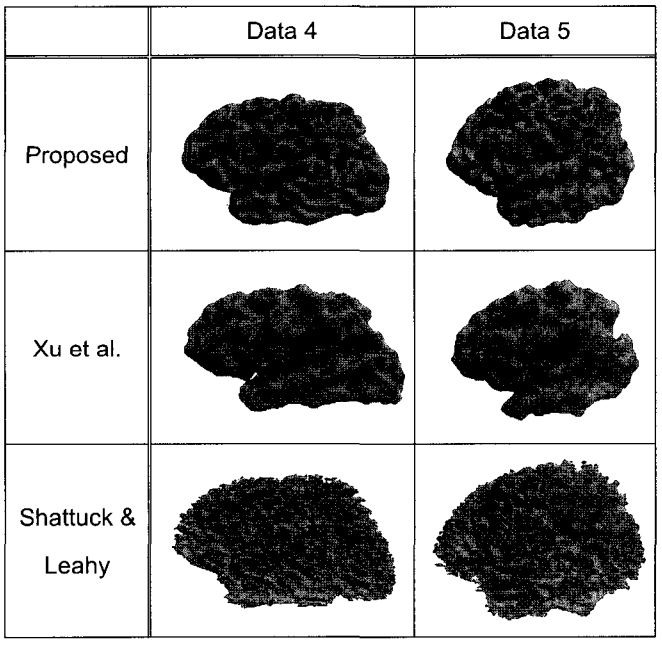

Fig. 26. The corrected surface in 3D of Data 4 and Data 5 by the algorithms of the proposed method, Xu et al., Shattuck and Leahy

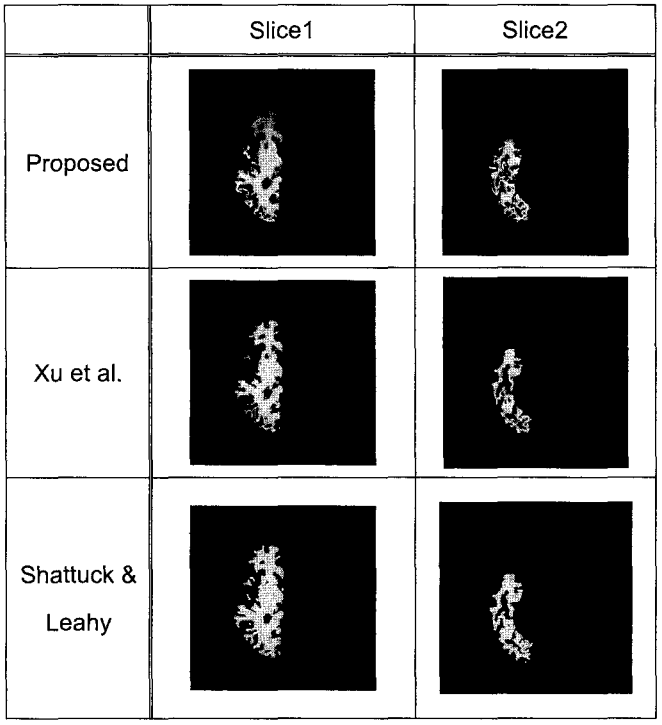

(a)

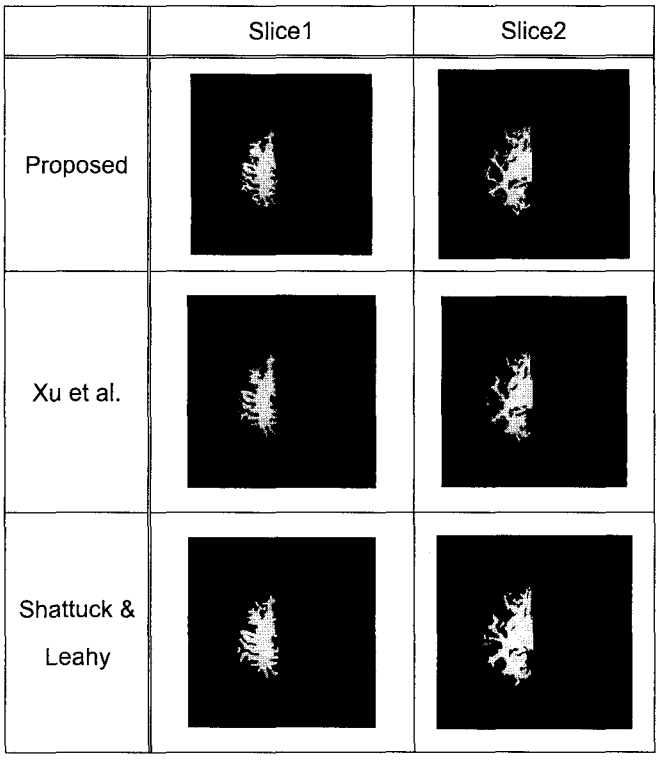

(b)

Fig. 27. The corrected surface in two slices by the algorithms of the proposed method, Xu et al., Shattuck and Leahy where the inside of the surface after removal of cavities and fractions shown in gray color: (a) Data 4 and (b) Data 5

The resultant surface by Shattuck and Leahy is not converged one. The corrected surface by Xu et al. is very smooth, however, surface by the proposed method has the gyri and sulci pattern sufficiently as shown in Fig.26. The corrected surface by the proposed method is not matched exactly to the object shown in two slices in Fig.27. This is probably because of the large internal force. Lowering of the internal force makes more intersection between vertices.

In Table 1, there are the number of faces and vertices of surface, *g*, and computation time before topology correction, after removal of fractions and cavities, and after removal of handles by the algorithms of Xu et al., Shattuck and Leahy, and the proposed method for Data 4 and Data 5. The corrected surface by Xu et al. and the proposed method has zero *g*. The computational time of the proposed method is smaller than the algorithm by Shattuck. Although the time of the proposed method takes longer than the algorithm by Xu et al., the appearance of the deformed surface looks better.

Table 1. The number of faces and vertices of surface, g, and computation time before topology correction, after removal of fractions and cavities, and after removal of handles by the algorithms of Xu et al., Shattuck and Leahy, and the proposed method for Data 4 and Data 5

	Data 4			
	# of Faces	# of Vertices	*g*	Time (*s*)
Before correction	371476	186018	-139	
Removal of fractions and cavities	364916	181856	302	34.2
Removal of handles				
Xu et al.	124248	62126	0	135
Shattuck & Leahy	362728	181018	174	1650
Proposed	81920	40962	0	250
	Data 5			
	# of Faces	# of Vertices	*g*	Time (*s*)
Before correction	294424	147478	-132	
Removal of fractions and cavities	285728	142418	224	32.1
Removal of handles				
Xu et al.	101668	50836	0	113
Shattuck & Leahy	283752	141716	81	1030
Proposed	81920	40962	0	241

CONCLUSION

The topological defects of the rendered surface of the segmented white matter and gray matter make geometrical distortion in flattening algorithms. Although there are several algorithms for topology correction, they usually fail to treat the deep and narrow concave region, thereby resulting in intersection or heavy computation amount. The proposed method for topology correction aims to solve these problems. Fractions and cavities are corrected by preserving only the set of vertices maximally connected. Handles are corrected using parametric deformable models in three steps. Based on two observations that there rarely is intersection if sphere is deformed to a surface with broad and shallow concave region and if deformation is performed between similar surfaces, the proposed method tries to reduce intersection between vertices. The proposed method deforms the vertices of a sphere model to the largely smoothed surface, to less smoothed surface, and so on until to the boundary surface between the segmented white matter and gray matter. Step 1 performs smoothing operation on the rendered surface. In Step 2, vertices of sphere are gradually deformed to the smoothed surfaces and finally to the boundary of the segmented white matter and gray matter. The Step 2 uses multi-resolutional approach to prevent the deep sulci from geometric intersection. In Step 3, 3D binary image is constructed from the deformed sphere of Step 2 and 3D surface is regenerated from the 3D binary image to remove intersection that may happen. Although the proposed method suffers from dependence on parameters, which is an intrinsic property of parametric deformable model, the resultant principle gyri and sulci patterns are almost preserved with small computation amount.

REFERENCES

[1] S. Ogawa, D.W. Tank, R. Menon, J.M. Ellermann, S. Kim, G.H. Merkle, and K. Ugurbil, *"Intrinsic signal changes accompanying sensory stimulation: functional brain mapping with magnetic resonance imaging"*, Proceedings of the National Academy of Sciences, Vol.89, pp.5951-5955, USA, 1992.

[2] P. Jezzard, P.M. Mattews, and S.M. Smith, Functional MRI: An Introduction to Methods, 1st Ed., OXFORD University press, pp.390, 2001.

[3] R. Goebel, and H. Jansma, Technical notes of BrainVoyager, ver.1.0, Brain Innovation, 2001.

[4] D.C. van Essen, H.A. Drury, S. Joshi, and M.I. Miller, *"Functional and structural mapping of human cerebral cortex: Solutions are in the surfaces"*, Proceedings of the National Academy of Sciences, Vol.95, pp.788-795, 1998.

[5] B. Fischl, M.I. Sereno, and A.M. Dale, *"Cortical Surface-Based Analysis II"*, NeuroImage, Vol.9, No.2, pp.195-207, 1999.

[6] D.W. Shattuck, and R.M. Leahy, *"Automated Graph-Based Analysis and Correction of Cortical Volume Topology"*, IEEE Trans. Medical Imaging, Vol.20, No.11, pp.1167-1177, 2001.

[7] C. Xu, D.L. Pham, M.E. Rettmann, D.N. Yu, and J.L. Prince, *"Reconstruction of the Human Cerebral Cortex from Magnetic Resonance Images"*, IEEE Trans. Medical Imaging, Vol.18, No.6, pp.467-480, 1999.

[8] M.J. Kwon, Y.J. Han, I.H. Shin, and H.W. Park, *"Hierarchical Fuzzy Segmentation of Brain MR Images"*, International Journal of Imaging Systems and Technology, Vol.13, No.2, pp.115-125, 2003.

[9] C. Montani, R. Scateni, and R. Scopigno, *"A modified look-up table for implicit disambiguation of Marching Cubes"*, The Visual Computer, Vol.10, No.6, pp.353-355, 1994.

[10] N. Kriegeskorte, and R. Goebel, *"An Efficient Algorithm for Topologically Correct Segmentation of the Cortical Sheet in Anatomical MR Volumes"*, NeuroImage, Vol.14, No.2, pp.329-346, 2001.

[11] X. Han, C. Xu, U. B-. Neto, and J.L. Prince, *"Topology Correction in Brain Cortex Segmentation Using a Multiscale, Graph-Based Algorithm"*, IEEE Trans. Medical Imaging, Vol.21, No.2, pp.109-121, 2002.

[12] J.-F. Mangin, V. Frouin, I. Bloch, J. Régis, J.L. –Krahe, *"From 3D Magnetic Resonance Images to Structural Representations of the Cortex Topography using Topology Preserving Deformations"*, Journal of Mathematical Imaging and Vision, Vol.5, pp.297-318, 1995.

[13] B. Fischl, A. Liu, and A.M. Dale, *"Automated Manifold Surgery: Constructing Geometrically Accurate and Topologically Correct Models of the Human Cerebral Cortex"*, IEEE Trans. Medical Imaging, Vol.20, No.1, pp.70-80, 2001.

[14] Guskov, and Z.J. Wood, *"Topological Noise Removal"*, Proceedings of Graphics Interface, pp.19-26, Ottawa, Canada, 2001.

[15] Z. Aktouf, G. Bertrand, and L. Perroton, *"A three-dimensional holes closing algorithm"*, Pattern Recognition Letters, Vol.23, pp.523-531, 2002.

[16] D.W. Shattuck, and R.M. Leahy, *"Topological refinement of volumetric data"*, Proceedings of the SPIE, Vol.3661, Medical Imaging 1999: Imaging Processing, pp.204-213, 1999.

[17] D. MacDonald, N.Kabani, D. Avis, and A.C. Evans, *"Automated 3-D Extraction of Inner and Outer Surface of Cerebral Cortex from MRI"*, NeuroImage, Vol.12, No.3, pp.340-356, 2000.

[18] P.C. Teo, G. Sapiro, and B.A. Wandell, *"Creating Connected Representations of Cortical Gray Matter for Functional MRI Visualization"*, IEEE Trans. Medical Imaging, Vol.16, No.6, pp.852-863, 1997.

[19] M. Kass, A. Witkin, and D. Terzopoulos, *"Snakes: Active Contour Models"*, Int'l J. Computer Vision, Vol.1, pp.321-331, 1987.

[20] A.K. Jain, Fundamentals of Digital Image Processing, Prentice Hall, Englewood Cliffs, New Jersey, pp. 569, 1989.

[21] L.D. Cohen, *"On Active Contour Models and Balloons"*, Computer Vision, Graphics, and Image Processing: Image Understanding, Vol.53, No.2, pp.211-218, 1991.

[22] M. Woo, J. Neider, and T. Davis, OpenGL Programming Guide: The Official Guide to Learning OpenGL, Version 1.1, 2nd ed. Addison Wesley Developers Press, pp.650, 1997.

[23] B. Leroy, *"Multi-Resolution algorithms for Active Contour Models"*, Proceedings of the 12nd International Conference on Analysis and Optimization of Systems, pp.58-65, 1996.